Clean Energy, 2023, Vol. 7, No. 3, 493–508
https://doi.org/10.1093/ce/zkac058
Advance access publication 2 May 2023
Research Article

Synergetic process between wind power and sewage sludge pyrolysis in a novel renewable-energy microgrid system

Chang Liu[1], Jiankun Zhuo[1,2], Yanfeng He[1], Shuiqing Li[1,*] and Qiang Yao[1,2]

[1]Key Laboratory for Thermal Science and Power Engineering of Ministry of Education, Tsinghua University, Beijing 100084, China
[2]Beijing Engineering Research Center for Ecological Restoration and Carbon Fixation of Saline–alkaline and Desert Land, Tsinghua University, Beijing 100084, China
*Corresponding author. E-mail: lishuiqing@mail.tsinghua.edu.cn

Abstract

To relieve the stress of sewage sludge (SS) disposal and effectively increase the use of renewable energy, a novel renewable-energy microgrid system (REMS) was developed, specifically designed to integrate a wind power plant (WPP) with energy storage and the SS pyrolysis process for heat and power generation. Based on a lab-scale pyrolysis experiment and 7-day numerical analysis, we studied the energy-recycling potential of SS and simulated the operational behaviours of REMS. According to the results, the calorific values of the pyrolytic gaseous and liquid products were better than those of the raw material, at 16.19 and 33.53 MJ/kg, respectively. The proposed REMS performed well in power supply and energy utilization with a design performance index of 99.23 when the WPP capacity was 200 $\mathrm{MW_e}$ and the initial wind-energy curtailment rate was 30%. It indicates that by converting SS into flammable gas, condensable liquid and carbon-rich solid residue, curtailed wind energy could be saved and the synergy between wind power and the SS pyrolysis process enabled the proposed microgrid system to effectively utilize renewable energy and provide reliable on-demand power service. The REMS installed with a 155-$\mathrm{MW_e}$ WPP achieved the optimal design in system performance, environmental benefit and construction cost under the initial wind-curtailment rate of 34.12%. The design scheme makes REMS capable of satisfying the 15.10-GWh power demand of end users and the 1700-t/day SS disposal need, and the curtailed wind energy could be reduced to zero.

Graphical Abstract

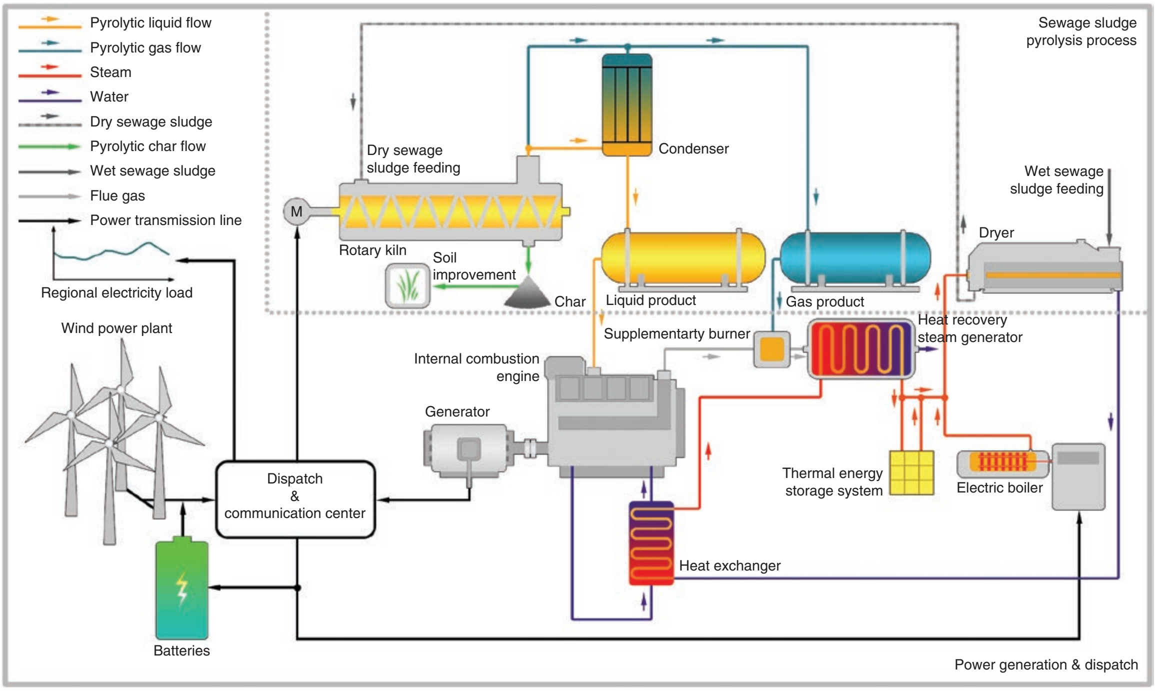

Keywords: sewage sludge; pyrolysis; wind power; microgrid; flexible operation

Received: 10 June 2022. **Accepted:** 21 October 2022

Introduction

As an inevitable solid by-product in municipal and industrial wastewater treatment, large volumes of sewage sludge (SS) contain multiple pollutants and bacteria [1, 2]. SS production in China has grown by an average of 10.7% per year since 2008, with an annual generation of 11.75 million tons of dry matter in 2019. The average production of SS in the USA and EU is ~17.8 million tons and 9.0 million tons of dry matter per year, respectively [3]. Therefore, SS is considered a threat to ecosystems. Systematic management and disposal of SS for protecting human health and the environment has become a critical concern worldwide. Typical sanitary landfills and sludge compost are believed to pose long-term risks to the surrounding environment and cannot meet stringent disposal standards [4, 5]. In this context, thermochemical conversion technologies, including incineration, pyrolysis and gasification, are gaining increasing attention as they convert non-recyclable SS waste into energy and valuable raw materials in environmentally safe ways [6, 7]. SS thermochemical conversion not only controls pollutants but also helps alleviate climate issues from fossil-fuel consumption [8].

Biomass and solid-waste incineration [9], pyrolysis [10] and gasification [11] are feasible in distributed energy systems and have great potential to increase renewable energy resources and mitigate fossil-fuel-driven greenhouse gas (GHG) emissions [12–14]. Bando *et al.* conducted a feasibility study on a microgrid system integrated with a municipal waste incinerator and showed that the waste heat from the incinerator plant could improve system reliability while avoiding resource waste at night [9]. Li *et al.* proposed a preliminary design of an independent solar-wind-biomass pyrolysis hybrid renewable-energy system for rural areas and verified the good potential for profit and carbon abatement [10]. Perna *et al.* considered the integration of waste gasification and electric energy-storage technologies in an advanced renewable-energy plant with attractive electricity production and storage efficiency [11]. Therefore, there is sufficient evidence to suggest that combining waste biomass-to-energy facilities with renewable-energy microgrids can provide reliable power management and proper waste management. Furthermore, Bora *et al.* demonstrated that renewable source-derived biofuels have not only environmental benefits, but also economic advantages in production costs, especially when municipal SS is used as the raw material [15].

To couple the disposal of SS with other renewable energy sources, there are two main ways to use renewable energy: pretreatment and process driving. Mechanical dewatering of SS and thermal drying are prerequisites for thermochemical disposal. These processes consume electricity or heat, leading to high disposal costs and even more GHG emissions. Renewable energy can power these pretreatment processes. Therefore, renewable energy is sometimes integrated as an energy source for SS drying in a wastewater treatment plant (WTP). Ameri *et al.* conducted a theoretical study on direct and indirect solar drying processes at a WTP and found that solar energy could reduce the moisture content of SS from 85.53 to 14.47 wt% [16]. Wang *et al.* developed a sandwich-shaped SS dryer model that worked with solar energy and mathematically simulated the efficiency of the system [17]. After 11 hours of continuously drying of SS with a thickness of 0.5 cm under artificial solar radiation at 500 W/m^2, the final water content was reduced to 5 wt%. However, solar radiation had a significant impact on the drying process, so stable SS drying could not be guaranteed because of solar-energy instability and operational disruptions at night. When renewable energy is used for process driving, it is equivalent to storing energy in the form of fuel production. Many studies have investigated the integration of sludge-to-energy (StE) systems with renewable driving energy. Li *et al.* performed a numerical simulation of a solar-driven SS steam gasification system to produce syngas with a high hydrogen content [18]. The fluidized-bed solar gasifier converted solar radiation into high-temperature heat and generated syngas after a series of thermochemical reactions. The hydrogen yield and the solar-to-fuel efficiency could be adjusted by modifying the gasifying agent composition and irradiance. However, the gasifier dynamic performance, which changed with solar radiation on longer timescales, was not discussed. Kokalj *et al.* also investigated the coupling of renewable power with gasification of SS, including gaseous product storage [19]. They calculated the process parameters suitable for the introduction of the gasified gaseous product into the natural gas supply network.

Although the technical feasibility of integrating StE technology and renewable energy has been tested, further research is still required on how to use StE to store flexible chemical energy and meet renewable electricity and heat supply demands. Previous studies have focused only on SS drying and conversion rather than its use as recovered energy. Furthermore, due to the heat demand during drying and thermochemical conversion processes, the most commonly selected energy source is solar or geothermal energy with natural heat-generating characteristics [20]. Other forms of renewable energy are rarely discussed in such research about multi-energy systems.

As the fastest-growing renewable-energy resource in China, wind energy accounted for 55.40% of total renewable generation in 2019, with 405.7 TWh accounting for nearly 50.96% of global renewable energy generation [21]. Due to the high variability of the wind, the mismatch between power supply and demand generally requires flexible regulation solutions (e.g. energy-storage technologies). Unlike wind and solar energy, which are variable by nature, energy extracted from waste biomass can be used for continuous and stable energy and converted into electricity, heat or other types of energy [22, 23]. Therefore, the StE processes driven by wind energy can store a certain amount of curtailed wind energy by producing biofuels and provide backup energy when the wind power is insufficient. This approach also helps solve high-costs problems of StE disposal problems in an eco-friendly way. Along with decades of development and industrial demonstration, pyrolysis is a highly versatile, advanced and economical waste-to-energy process [24–26]. During pyrolysis, feedstocks are decomposed into fractions of flammable gases, condensable liquids and carbon-rich solid residues [27]. These pyrolysis products can be used for power generation, district heating and soil remediation. Combining the advantages of wind energy and recycling the waste energy of wastewater sludge, a novel microgrid system could be developed. However, the complementary mechanisms of the two types of renewable energy and different types of energy storage should be studied further.

Therefore, this study proposed a wind-energy system integrated with SS disposal based on pyrolysis technology by (i) analysing the coupling mechanism between StE technology, intermittent renewable energy and energy storage and (ii) studying the operational flexibility and environmental benefits of the integrated system. To this end, SS pyrolysis experiments were conducted to study SS pyrolytic properties and establish an SS pyrolysis process model based on mass and energy balances. The proposed integrated system was numerically simulated using the Modelica language. We investigated the overall system performance and the key parametric design method. We also evaluated environmental benefits to further optimize the design. This work improves our understanding of the synergistic and complementary effects between the thermochemical conversion process of solid waste and intermittent renewable energy, especially the renewable energy source without the features of natural heat generation. Furthermore, the proposed integrated power system provides new ideas for the large-scale and innovative application of renewable energy.

1 System description

A renewable-energy microgrid system (REMS) equipped with a wind power plant (WPP) and SS pyrolysis process was developed for electricity generation and SS disposal. Two key energy sources constituted the integrated system: wind and sewage sludge. The total electricity demand of the proposed microgrid consisted of three parts: (i) the electrical load for the regional power supply, (ii) the drying energy consumption and (iii) the energy consumption to drive pyrolysis. The connections between each of the proposed microgrid system facilities are shown in Fig. 1. The pyrolysis liquid product (PL) was used to generate electricity through an internal combustion engine (ICE). And a heat-recovery steam generator (HRSG) was configured at the ICE outlet to recover the heat from the combustion gases. The combined heat and power ICE (ICE-CHP) system shared the electrical load with the WPP. At the same time, ICE-CHP steam was transferred to the dryer where wet sludge with a moisture content of >80 wt% was dried to <10 wt%. An electric boiler (EB) was designed to convert wind power into heat for steam drying. A thermal energy-storage (TES) system was used to help smooth thermal energy fluctuations due to wind power. This could be any easy-to-control and low-cost TES device, e.g. sensible heat storage with liquid and solid heat-transfer medium. The pyrolysis incondensable gas (PG) augmented drying heat in the supplementary HRSG burner. When wind power exceeded the electricity demand, both PL and PG were stored in bio-oil and biogas storage tanks, respectively, without being involved in power regulation. An electricity-storage system using batteries regulated the electrical power. To achieve safe and flexible operations with reliable on-demand power supply, a power dispatch and communication centre (PDCC) controlled the REMS. Moreover, the integrated system included backup power for SS pyrolysis from the utility grid, which ensured uninterrupted SS disposal. Pyrolytic char was utilized for soil remediation to increase the system economy.

As wind power fluctuated with the wind speed and electrical load fluctuated with time, there were mismatches between power output and power load. PL and batteries improved power quality. The control strategies of the microgrid system are described below:

- The system was able to continuously pyrolyse a specific mass of SS at a steady rate every day, resulting in steady production rates of gas, liquid and solid products. Then, PL and PG were stored in the bio-oil and gas tanks at constant flow rates, and pyrolytic char was collected for later soil remediation. At the same time, the wet SS was dried at a constant rate to a moisture content of <10 wt% to keep the system running the next day. The drying power was also set to be constant for 24 hours.
- In the PDCC, a two-step energy allocation decision process was implemented. The first step was to determine whether the wind-power output matched the power load. If wind power was equal to the on-demand power, the ICE-CHP system and batteries were on standby. If wind power was not enough to meet the power demand, the electricity gap

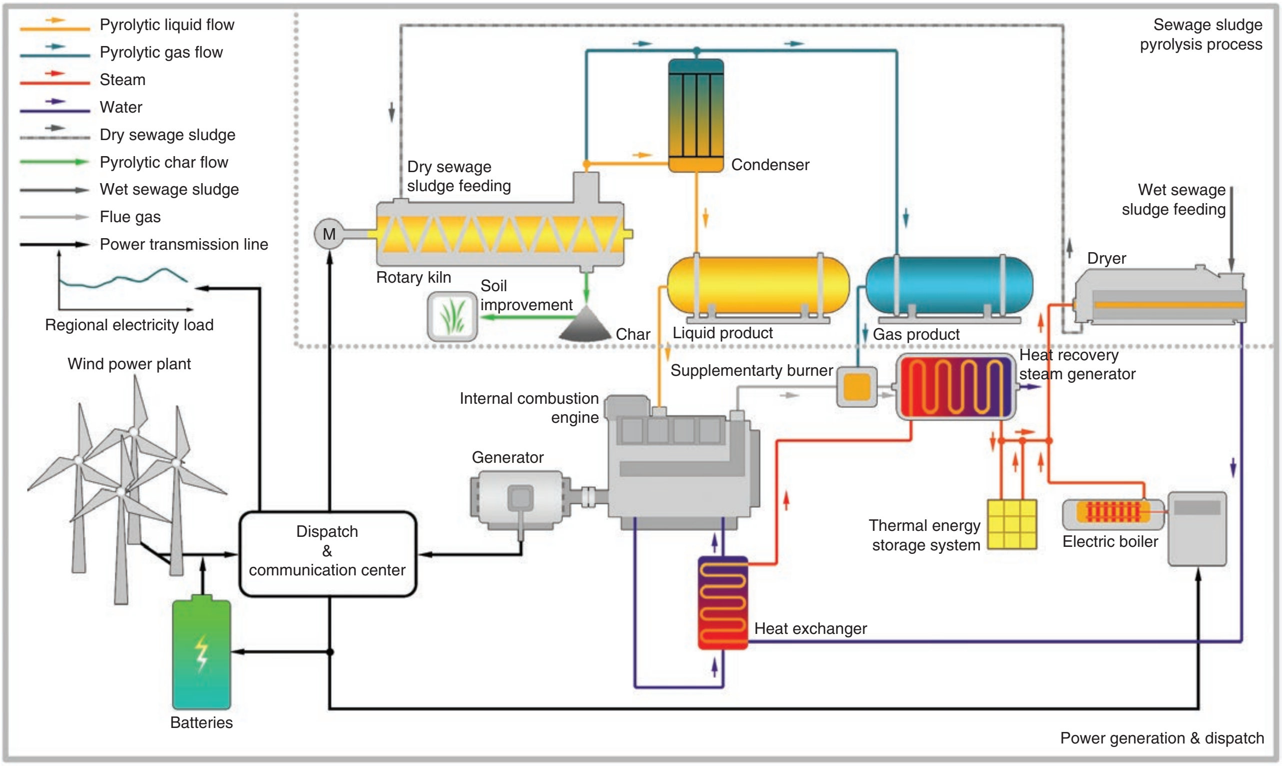

Fig. 1: System structure of the REMS.

was met by the ICE output and battery discharge, but the PL preferentially met the electricity demand. Once the wind-power output exceeded the power demand, excess wind energy was stored and the ICE-CHP remained idle. In the second decision step, the HRSG thermal output was compared to the drying-heat load. If the thermal power was equal to the drying power, the PG was stored at a uniform storage rate. When the HRSG thermal output exceeded the drying power, the excess heat was stored in the thermal storage system. When the thermal power was lower than the drying power and there was no thermal energy left in the thermal storage system, PG was introduced to the supplementary burner to compensate for the insufficient heat output. If there was still a heat shortage for the SS dryer, the EB was put into operation to achieve on-demand heat.

- The systems gave priority to SS disposal. The aim of REMS was not only meet the power demand but also to improve the energy efficiency. If the total renewable-energy output did not meet the energy requirements, the needed electricity could be purchased from the power grid.

2 System model and assumptions

A system model was established to simulate the operational behaviours of each REMS device using the open-source Modelica library WindPowerPlants [28]. The system control scheme is shown in Fig. 2. Here, we make assumptions so as to simplify the simulation study:

- We assumed that the response rate, capacity and charge and discharge frequency modes of every energy-storage device could be achieved through reasonable design and cascade configuration.
- The specific electrical load, wind-speed curves and SS pyrolysis experimental results were used to determine the operational behaviour. The wind power P_{wind} generated from the given wind speeds can be calculated by using the system model and the end-user electrical load was assumed to be identical every day and copied to a diurnal curve. The SS pyrolysis energy-transformation model was established according to experimental results in a lab-scale pyrolysis set-up. The net energy input required in the process was regarded as the driving energy, which deducted the heat dissipation from the energy input in the experiment and was scaled up proportionally in the REMS.
- When REMS electricity and heat generation were sufficient, the system provided good load-following.
- We adopted the fixed power-generation efficiency $\eta_{ICE,e}$ to calculate the electrical power output from the ICE-CHP. To avoid frequent ICE starts and stops caused by peaking operation, the running time was set to last for ≥1 hour after

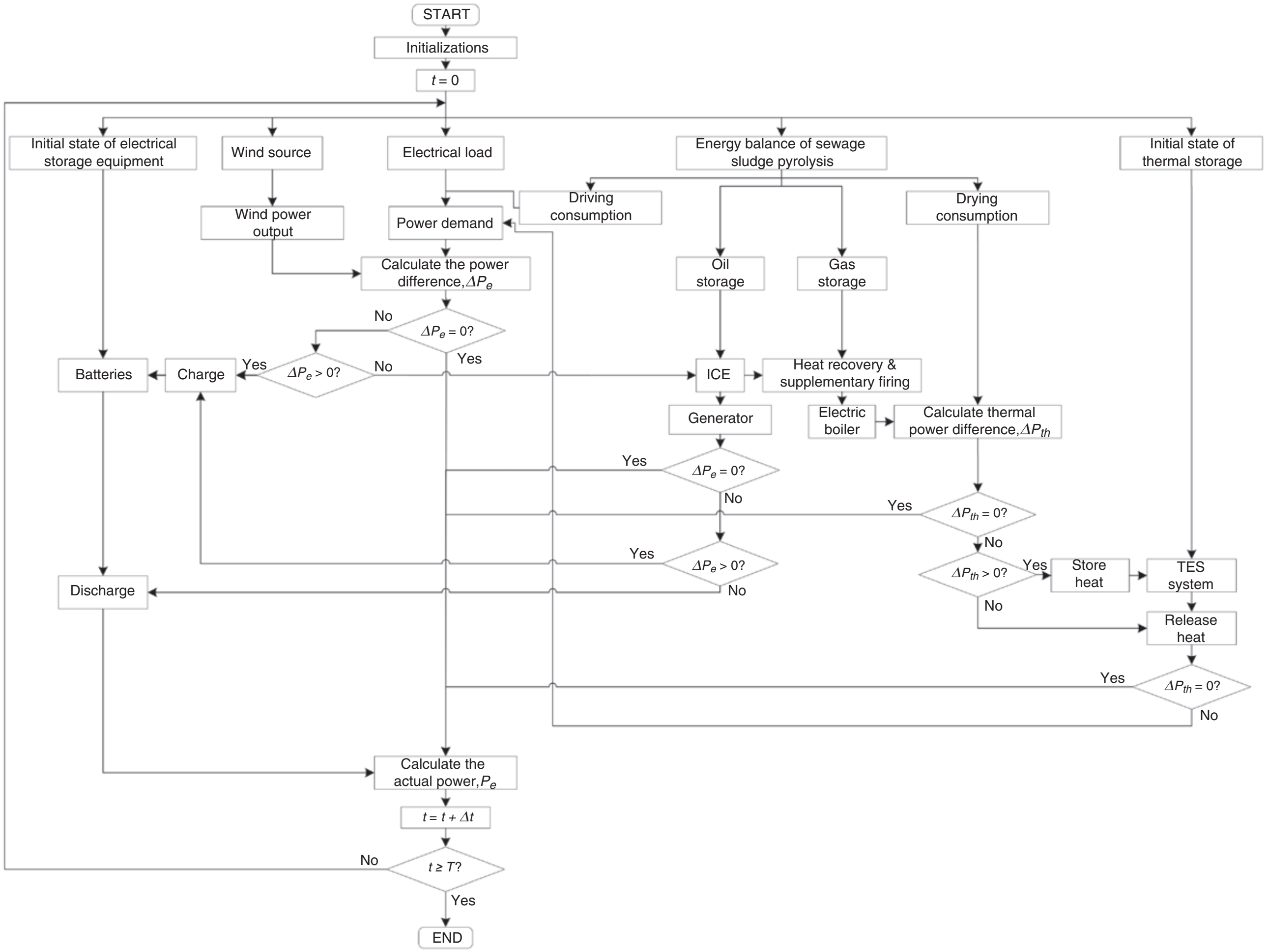

Fig. 2: Flow chart on the control scheme of the REMS.

each start. Fuel was purchased since the PL may have been inadequate. During the running period, once the accumulated PL was used up or the wind power was enough for the electricity supply, the ICE was turned down to the minimum generation. The efficiencies η_{HRSG} and η_{EB} were estimated for HRSG recovery heat and EB heat generation, respectively. Thus, total energy demand, including the electrical load and SS drying and pyrolysis energy consumptions, led the REMS to obtain the planned power and heat generation, $P_{demand,e}$ and $P_{demand,th}$.

The power gaps were calculated by the imbalance between power supply and demand. The power and heat gaps directly affected the operational decisions (charge or discharge) of each storage unit. Finally, we determined the actual operational REMS output and the performance of the system.

3 Evaluation of integrated renewable-energy microgrid systems

3.1 System evaluation indexes

In this study, both the operational performance of the REMS and the impact of its configuration on the economy and the environment were the most important issues in evaluating the feasibility of integrating renewable-energy management with the disposal of SS.

3.1.1 *System performance*

The REMS-energy distribution was determined according to the system operation strategy and assumptions in Sections 1 and 2. Energy utilization and power-supply capacity could be mathematically expressed as follows. First, the power demand can be calculated by using Equation (1):

$$P_{demand,e} = P_{load,e} + P_{pyr} + P_{EB,e,input} \tag{1}$$

where $P_{load,e}$, P_{pyr} and $P_{EB,e,input}$ are the electrical load, the pyrolytic driving energy and the electrical consumption, respectively. Then, the behaviours of the ICE and storage device can be determined by the power gap between the wind-power output and the demand, and the power gap (ΔP_e) can be obtained by using Equation (2):

$$\Delta P_e = P_{wind} - P_{demand,e} \tag{2}$$

When ΔP_e is negative, ICE needs to be run to make up for the shortfall in power supply and smooth the power fluctuations. If the ICE is turned on, the expressions of electrical power are as follows:

$$P_{ICE,e} = \begin{cases} |\Delta P_e|, & (\Delta P_e < 0, S_{PL} > 0, P_{ICE,e,\min} \le |\Delta P_e| \le P_{ICE,e,\max}) \\ P_{ICE,e,\max}, & (\Delta P_e < 0, S_{PL} > 0, P_{ICE,e,\max} \le |\Delta P_e|) \\ P_{ICE,e,\min}, & (\Delta P_e < 0, S_{PL} = 0) \\ P_{ICE,e,\min}, & (\Delta P_e > 0, T_{ICE} \le 1 hour) \end{cases} \tag{3}$$

where $P_{ICE,e}$ is the electrical generation, and $P_{ICE,e,\max}$ and $P_{ICE,e,\min}$ represent the maximum and minimum ICE power output, respectively. S_{PL} denotes the reserve of PL and T_{ICE} denotes the running time of the ICE after each start. Equation (4) describes the relationship between the electrical power output and the consumption of PL:

$$P_{ICE,e} = \eta_{ICE,e} \frac{\partial \left(H_{fuel,PL} M_{fuel,PL}\right)}{\partial t}, (0 \le P_{ICE,e} \le P_{ICE,e,\max}) \tag{4}$$

where $\eta_{ICE,e}$ is the efficiency of the ICE power generation, and $H_{fuel,PL}$ and $M_{fuel,PL}$ are the calorific value and mass used for power supply. PL shortage might occur during the 1-hour operation. When the PL consumption rate is higher than the production rate, additional fuel purchases will be needed:

$$M_{fuel,pur} = \frac{H_{fuel,PL} M_{fuel,PL} - H_{fuel,PL} Y_{PL} M_{SS}}{H_{fuel,pur}} \tag{5}$$

where Y_{PL} denotes the PL yield and M_{SS} denotes the disposed SS mass. $M_{fuel,pur}$ and $H_{fuel,pur}$ are the mass and calorific value of the purchased fuel.

The heat demand $P_{demand,th}$ was determined by the energy consumption P_{drying} during the SS drying process. There were three heat sources that collectively for thermal demand: one from ICE heat recovery, one from the PG supplementary combustion (SCPG) and the last from the EB. The first two parts constituted the HRSG heat output. When the ICE was in operation, all the heat recovered from its flue gas and cooling water was transferred to the SS dryer and the TES. The difference between the total recovered ICE heat and the drying load was defined as the parameter ΔP_{th} to make decisions on the following TES operation strategies and the other two heat sources. These energy relationships are derived from Equations (6–8):

$$P_{demand,th} = P_{drying} \tag{6}$$

$$\Delta P_{th} = P_{ICE,th} - P_{demand,th} \tag{7}$$

$$|\Delta P_{th}| = \begin{cases} P_{charge,TES}, & (\Delta P_{th} > 0) \\ P_{charge,TES}, & (\Delta P_{th} < 0, SOC_{TES} > SOC_{TES,\min}) \\ P_{SCPG,th}, & (\Delta P_{th} < 0, SOC_{TES} \le SOC_{TES,\min}, \\ 0 < P_{SCPG,th} \le P_{SCPG,th,\max}) \\ P_{SCPG,th} + \eta_{EB} P_{EB,e,input}, \\ (\Delta P_{th} < 0, SOC_{TES} \le SOC_{TES,\min}, \\ 0 < P_{SCPG,th} = P_{SCPG,th,\max} < |\Delta P_{th}|) \end{cases} \tag{8}$$

where $P_{ICE,th}$ is the recovered ICE heat. $P_{charge,TES}$ and $P_{discharge,TES}$ represent the stored and released heat. SOC_{TES} is defined as the charge state of the TES system. If $SOC_{TES} = 1$, the TES is fully charged, and if $SOC_{TES} = 0$, the TES system is completely discharged. $SOC_{TES,\min}$ denotes the minimum effective heat-accumulation amount, which means that the TES system cannot be used efficiently for heating when the stored heat is less than $SOC_{TES,\min}$. $P_{SCPG,th}$ is the heat from PG combustion in the HRSG and $P_{SCPG,th,\max}$ represents the maximum value of $P_{SFPG,th}$. η_{EB} is given as the EB efficiency.

$P_{ICE,th}$ has a coupling relationship with the electrical generation of the ICE and can be calculated with the ICE and HRSG efficiencies:

$$P_{ICE,th} = \frac{(1 - \eta_{ICE,e}) \eta_{HRSG} P_{ICE,e}}{\eta_{IEC,e}} \tag{9}$$

The SOC_{TES} depends on the ratio of the net stored energy to the capacity of the TES system, which is expressed as:

$$SOC_{TES} = \frac{E_{TES,net}}{I_{Cp,TES}} \tag{10}$$

The stored and released heat of each storage period can be calculated by using Equations (11) and (12):

$$\Delta E_{charge,TES,j} = \int_{T_j} P_{charge,TES} dt \tag{11}$$

$$\Delta E_{discharge,TES,k} = \int_{T_k} P_{discharge,TES} dt \tag{12}$$

where T_j and T_k represent the length of time of the j-th and k-th (j = 1, 2, 3, …, n and k = 1, 2, 3, …, m) storage (release) periods. Then the TES capacity $I_{Cp,TES}$ is given as the maximum value of $\Delta E_{charge,TES,j}$ so that the TES system can take the recovered HRSG waste heat:

$$I_{Cp,TES} = \max(\Delta E_{charge,TES,j}) = \tag{13}$$

Taking into account the entire operational time T ($T \geq T_j$), the total stored and released heat from the TES system can be determined as follows:

$$E_{charge,TES} = \int_T P_{charge,TES} dt \tag{14}$$

$$E_{discharge,TES} = \int_T P_{discharge,TES} dt \tag{15}$$

At moment $t = t_c$ of the operation period, $E_{TES,net}$ can be calculated using Equation (16):

$$E_{\mathrm{TES},net|t=t_c} = \mathrm{SOC}_{\mathrm{TES}|t=0} I_{Cp,TES} + \int_{t_c} P_{charge,TES} dt - \int_{t_c} P_{discharge,TES} dt \tag{16}$$

If the recovered ICE heat cannot meet the drying requirement, PG will be used through supplementary combustion. The PG mass used to make up the heating gap can be calculated as follows:

$$M_{fuel,PG} = \frac{\int_T P_{\mathrm{SCPG},th} dt}{\eta_{\mathrm{HRSG}} H_{fuel,PG}} \tag{17}$$

where $H_{fuel,PG}$ is the calorific value.

Finally, the charge and discharge powers of the batteries can be calculated as in Equations (18) and (19):

$$P_{charge,B} = \begin{cases} \Delta P_e, & (\Delta P_e > 0, \mathrm{SOC_B} < 1) \\ 0, & (\Delta P_e > 0, \mathrm{SOC_B} = 1) \\ 0, & (\Delta P_e < 0) \end{cases} \tag{18}$$

$$P_{discharge,B} = \begin{cases} 0, & (\Delta P_e > 0) \\ 0, & (\Delta P_e < 0, P_{\mathrm{ICE},e} = |\Delta P_e| \, or \mathrm{SOC_B} \leq \mathrm{SOC_{B,min}}) \\ |\Delta P_e| - P_{\mathrm{ICE},e}, & (\Delta P_e < 0, \mathrm{SOC_B} > \mathrm{SOC_{B,min}}, P_{\mathrm{ICE},e} < |\Delta P_e|) \end{cases} \tag{19}$$

where SOC_B denotes the state of charge of the batteries and $\mathrm{SOC}_{B,\min}$ denotes the minimum effective charged energy. SOC_B is defined by Equation (20):

$$\mathrm{SOC_B} = \frac{E_{\mathrm{B},net}}{I_{Cp,\mathrm{B}}} \tag{20}$$

where EB,net and $I_{Cp,B}$ represent the energy left in the batteries at a certain moment ($t = t_c$) and the configured battery capacity. $E_{B,net}$ can be calculated by using Equation (21):

$$E_{\mathrm{B},net|t=t_c} = \mathrm{SOC}_{\mathrm{B}|t=0} I_{Cp,\mathrm{B}} + \int_{t_c} P_{charge,B} dt - \int_{t_c} P_{discharge,B} dt \tag{21}$$

The configured battery capacity had a great influence on the overall energy utilization and operational safety of the integrated system. Capacity design optimization was required because a battery that is too small cannot improve power quality and reduce the power-supply capability, while a battery that is too large will increase investment and maintenance costs. The energy charged and discharged by batteries during each charge and discharge period (T_l and T_h, $l = 1, 2, 3, \ldots, p$ and $h = 1, 2, 3, \ldots, q$) can be calculated by using Equations (22) and (23):

$$\Delta E_{charge,B,l} = \int_{T_l} P_{charge,B} dt \tag{22}$$

$$\Delta E_{discharge,B,h} = \int_{T_h} P_{discharge,B} dt \tag{23}$$

On the basis of the system power demand, the minimum battery capacity configuration could be obtained using the following calculation method. When the total wind energy meets the electricity demand and the accumulation of charge energy is just enough to satisfy the accumulated discharge energy, the maximum $\Delta E_{discharge,B,h}$ value is considered the minimum configured battery capacity. When the total wind generation cannot meet the electricity demand, the maximum $\Delta E_{charge,B,l}$ value is the minimum battery capacity. In this context, the minimum capacity of the batteries is given as:

$$I_{Cp,\mathrm{B},\min} = \begin{cases} max(\Delta E_{discharge,B}), \quad (\int_T P_{wind} dt \geq \\ \int_T P_{demand,e} dt, \mathrm{SOC}_{\mathrm{B}|t=0} I_{Cp,\mathrm{B},\min} + \\ \int_T P_{charge,B} dt = \int_T P_{discharge,B} dt) \\ max(\Delta E_{charge,B}), \quad (\int_T P_{wind} dt < \int_T P_{demand,e} dt) \end{cases} \tag{24}$$

It should be noted that when the total wind-energy generation in REMS cannot meet the EB electricity requirement, the power purchased from the power grid (P_{grid}) will be needed. Thus, the actual electrical power output of the REMS can be calculated using Equation (25):

$$P_{act,e} = \begin{cases} P_{demand,e}, & (\Delta P_e \geq 0) \\ P_{wind} + P_{\mathrm{ICE},e} + P_{discharge,B} + P_{grid}, & (\Delta P_e < 0) \end{cases} \tag{25}$$

Therefore, three key parameters for the evaluation of the system can be obtained, including the electricity supply completion rate (CR), the energy-utilization rate and the design performance index. The REMS CR is defined as:

$$\delta_{\mathrm{E}} = \frac{\int_T P_{act,e} dt}{\int_T P_{demand,e} dt} \times 100\ \% \tag{26}$$

The REMS-energy utilization rate can be calculated by using Equation (27):

$$\delta_{\mathrm{U}} = \frac{\int_T P_{act,e} dt + E_{\mathrm{B},net} + \int_T P_{demand,th} dt + E_{TES,net}}{\int_T P_{wind} dt + E_{\mathrm{StE}} + E_{pur,total} + \mathrm{SOC}_{TES|t=0} I_{Cp,TES} + \mathrm{SOC}_{\mathrm{B}|t=0} I_{Cp,\mathrm{B}}} \times 100\ \% \tag{27}$$

where $E_{pur,total}$ is the actual purchased energy caused by the system operational strategies. E_{StE} is the total energy converted from PL and PG. $E_{pur,total}$ and E_{StE} are given as:

$$E_{pur,total} = \int_T P_{grid} dt + H_{fuel,pur} M_{fuel,pur} \tag{28}$$

$$E_{\mathrm{StE}} = H_{fuel,PL} M_{fuel,PL} - H_{fuel,pur} M_{fuel,pur} + H_{fuel,PG} M_{fuel,PG} \tag{29}$$

The design performance index assesses the REMS design scheme rationality:

$$\Omega_{\ design} = \delta_{\mathrm{E}} \delta_{\mathrm{U}} \times 100 \tag{30}$$

In a certain power demand, an excessively large design capacity of each unit may lead to a reduction in the energy-utilization rate. However, an excessively small design capacity of each unit would decrease the power-supply CR. The optimal REMS design can be obtained when the CR and the energy-utilization rate reach the maximum.

3.1.2 *Environmental and economic benefits*

Due to logistical and environmental safety concerns, SS disposal generally suffers from high operating costs [29]. For example, landfilling SS costs $75 per wet ton [30]. However, REMS enables the clean disposal of SS and energy reuse and forms a circular economy. Commonly, governments adopt financial subsidies for sludge disposal and biochar soil remediation also improves financial and environmental benefits. Raw SS volatiles can replace a considerable amount of fossil-energy resources. Integrated batteries and ICE are also helpful in mitigating CO_2 emissions from conventional coal-fired plants. The monetized social damage of

CO_2 emissions was estimated at ~$46 per ton in 2017 [31]. Other GHGs, including methane, nitrous oxide and hydrofluorocarbons, usually convert their social costs into CO_2-equivalent units in economic research, but this was not covered in this study due to research limitations. Based on the assumption of maintaining the energy demands of SS pyrolysis and the operational strategy of the system, the additional costs of CO_2 emissions were a negative term in the environmental benefit. The monetized environmental value of REMS can be estimated by using Equation (31):

$$C_{env} = C_{subsidy} + C_{soil} + C_{emission} \tag{31}$$

The terms $C_{subsidy}$, C_{soil} and $C_{emission}$ define the financial SS disposal subsidies, soil-remediation benefits and the monetized CO_2 emission-mitigation benefits, respectively. These terms are expressed as:

$$C_{subsidy} = c_{subsidy} M_{SS} \tag{32}$$

$$C_{soil} = c_{soil} \eta_{soil} M_{char} \tag{33}$$

$$C_{emission} = c_{emission} M_{CO_2} \tag{34}$$

where $c_{subsidy}$, c_{soil} and $c_{emission}$ represent the SS unit mass disposal subsidy, the effective soil-remediation unit cost and the CO_2 emissions unit cost. M_{SS} and M_{char} are the masses of disposed SS and pyrolytic char. η_{soil} is defined as the effective coefficient of pyrolytic char. M_{CO2} is the reduction in total CO_2 emissions during the operation period and can be calculated by using Equation (35):

$$M_{CO_2} = \zeta_e \left(\int_T P_{demand,e} dt - \int_T P_{grid} dt \right) - \zeta_{fuel,pyr} \sum_i \left(H_{fuel,i} M_{fuel,i} \right) - \zeta_{fuel,pur} H_{fuel,pur} M_{fuel,pur} \tag{35}$$

where ζ_e, $\zeta_{fuel,pyr}$ and $\zeta_{fuel,pur}$ denote the CO_2 emission factors per unit of energy consumption of electricity, pyrolytic fuels and purchased fuel. The parameters $H_{fuel,i}$ and $M_{fuel,i}$ are the calorific value and mass, respectively, where the subscript i = PL and PG.

The F_{REMS} parameter is given to demonstrate the influence of REMS revenue and expenditures on the system economic benefits, which changes with the installed WPP capacity and wind speed:

$$F_{REMS} = C_{cons} + C_{sell} - C_{pur} \tag{36}$$

where C_{cons} consists of the construction costs of the WPP, SS drying and pyrolysis systems, ICE-CHP system, EB and storage devices. C_{sell} denotes the total income from the sale of electricity, pyrolysis fuels and pyrolytic char. C_{pur} represents the total expense of purchasing fuel and electricity from the grid for energy shortages. We ignored the impacts of electricity prices on the transaction between the microgrid and the utility grid in this study. However, when the power-supply CR reaches 100%, C_{cons} and C_{sell} can be simplified as Equations (37) and (38). Because the scales of the pyrolysis reactor, ICE-CHP system, EB and fuel storage tanks are fixed and the electricity to be sold and the mass of char used for soil remediation are constant, the six terms do not affect the F_{REMS} trends.

$$C_{cons} = c_{wind} I_{Cp,wind} + c_B I_{Cp,B} + c_{TES} I_{Cp,TES} \tag{37}$$

$$C_{sell} = c_{fuel,pyr} \sum_i H_{fuel,i} M_{fuel,i,sell} \tag{38}$$

C_{pur} is defined as:

$$C_{pur} = c_{fuel,pur} H_{fuel,pur} M_{fuel,pur} + c_e \int_T P_{grid} dt \tag{39}$$

where c_{wind} is the capital cost of the WPP and $I_{Cp,wind}$ is the installed WPP capacity. c_B and c_{TES} are the capital costs of the battery and TES systems. $M_{fuel,i,sell}$ represents the redundant fuel mass i. $c_{fuel,pyr}$ and $c_{fuel,pur}$ represent the redundant pyrolytic fuel and the extra-purchased fuel prices, and c_e represents the electricity price.

3.2 Case settings

3.2.1 SS pyrolysis experiment

Although SS compositions differ from one place to another and change over time, there are some common characteristics, such as high content of heavy metals, low-calorific values and characteristic similarities with biomass fuel. Theoretically, the pyrolysis process refers to the decomposition of hydrocarbons. The SS properties, the composition and yield, and the mass and energy balances are necessary to evaluate the potential for SS recycling. This subsection provides detailed information from lab-scale pyrolytic experiments. The SS sample proximate and ultimate analyses are tabulated in Table 1.

SS pyrolysis experiments were conducted in a continuous rotary kiln reactor system developed by Tsinghua University and Steinbeis-Transferzentrum fuer Verfahrens-, Energie-und Umwelttechnik because of our good experimental equipment and research experience. In addition, the rotary kiln is suitable for the treatment of solid and liquid waste of different shapes and has been widely applied in mechanical, physical and chemical processes with high technical maturity, simple operation and high controllability. The feedstock residence time can be easily adjusted during the slow inclined kiln rotation to ensure good sludge feedstock mixing and uniform pyrolytic products can be achieved due to good heat transfer and a wide operating temperature range. A schematic diagram of the continuous rotary kiln reactor system was illustrated in previous work [34]. The key feature of the reactor system is the horizontally arranged rotary kiln reactor chamber, in which reciprocating feed motion can be realized by programmable special lamina control. Table 2 lists the experimental parameters. The final pyrolysis

Table 1: Characteristics of the wastewater sludge sample and physical properties

Parameters	Value
Mechanical dewatered SS	
Moisture content, wt%	80
Dried SS	
Moisture content, wt%	6.26
Ash, wt%	35.51
Volatile matter, wt%	56.86
Fixed carbon, wt%	1.37
Calorific value[a], MJ/kg	13.55
C, wt%, daf	33.06
H, wt%, daf	4.69
O, wt%, daf	24.83
N, wt%, daf	5.36
S, wt%, daf	0.84
Latent heat of water, kJ/kg	2090
Specific heat of water, kJ/(kg°C)	4.18
Specific heat of dried SS [32], kJ/(kg°C)	1.95

[a] By the Dulong formula [33], i.e. Calorific value = 0.3383C wt% + 1.443(H wt% – O wt%/8) + 0.0927S wt%. daf, dry ash-free.

temperature was set at 550℃, which can maintain a high level of volatile matter release [35, 36]. The feed rate was set at 1 kg/h with a sample size distribution of 0.02~0.04 that was fed into the reactor at periodic intervals. Argon gas was continuously pumped into the system to maintain an inert atmosphere. Argon was also used as the carrier gas to remove the volatile components from the pyrolysis reactor.

3.2.2 *REMS operation and performance*

This subsection describes the preliminary performance of the REMS from a system perspective, mainly based on energy management and dispatch control. We conducted a 1-week REMS simulation to study the system power supply and SS disposal performance, based on the wind speeds that fully demonstrate the randomness and volatility of the WPP.

The daily amount of SS pyrolysis in this simulation work was close to the yield of a coastal city of China with a permanent population of >9 million. The 7-day wind speed during the operation period is shown in Fig. 3, with a time interval of 10 minutes. To account for wind fluctuation, the WPP was set to 200 MWe, so the WPP maximum planned wind power could be twice as high as the maximum regional electrical load. The calculated planned wind power and the electrical load are illustrated in Fig. 4. The electrical load experienced a maximum peak (at 7:15 p.m.) and a minimum trough (at 2:45 a.m.) during each day. Analysing and establishing the balance of power supply and demand was essential to ensure the reliability and stability of the microgrid. Without the aid of the energy-storage system (ESS), the energy exceeding the demand power was curtailed. The ratio of the curtailed energy to the total available wind energy was defined as the curtailment rate of wind energy φ_{cur}. The initial set value of φ_{cur} was 30%. Under this scenario, the CR of the electricity supply (δ_E) was 88.66% and the design performance index (Ω_{design}) was 62.06. A 200-MW$_e$ WPP with an electricity-storage system was numerically investigated to better compare the performance of the REMS design. The wind-energy curtailment rate, CR and design performance index were 19.44%, 100% and 82.19, respectively. According to the matches between the planned wind power and electrical load in Fig. 4, the ICE and EB capacities were fixed at 50 MW$_e$ and 40 MW$_t$. Table 3 lists the efficiency of each unit and other REMS design parameters.

Table 2: Experimental conditions of the rotary kiln reactor

Parameter	Value
Length of reactor chamber, mm	760
External diameter of reactor chamber, mm	134
Final pyrolysis temperature, °C	550
Temperature of material outlet, °C	400
Pressure of reactor chamber, bar	−3
Residence time of solid feedstock, min	60

3.2.3 *REMS initial wind-curtailment rate and WPP scale*

Wind quality had a significant impact on the CR of the electricity supply and the wind-energy utilization rate. When the wind speed was quite low, the difference between electricity supply and demand was large, resulting in a power shortage and a small REMS wind-curtailment rate. If the wind speed gradually increased, the matching degree between electricity supply and demand increased and the power-supply CR increased accordingly. When the wind speed reached 8.5 m/s, the electricity supplied by the WPP exceeded the demand. The higher wind speeds led to a quite high wind-curtailment rate without any energy-storage aid. Therefore, the initial wind curtailment reflected the match between electricity supply and demand. The configured WPP capacity also influenced the system performance, i.e. the energy-utilization rate and the energy-supply CR. Therefore, we conducted a parametric study of different wind-curtailment rates and WPP scales to investigate their influence on the performance of REMS, as shown in Table 4. In each case, the initial curtailment rate started at 10% and increased to 50% in increments of 10. It should be noted that the initial wind-curtailment rate was limited by the WPP construction scale, and the maximum wind curtailments of the four studied cases were 28.07%, 40.07%, 48.61% and 50%. The wind speed of each case was fitted with a Poisson distribution when under the same WPP capacity.

3.2.4 *REMS environmental and economic analysis*

Table 5 lists the expenses involved and equipment costs. The monetization was estimated according to the definition in Subsection 3.1.2. The reduction in CO_2 emissions was also calculated compared with the conventional coal-fired power plant. Normally, the energy-production costs decrease with the configured system scale, but we estimated the price of pyrolysis fuel products based on the fixed production cost of $9.88/GJ [37].

4 Results and discussions

4.1 Analysis of the pyrolysis experiment

In the microgrid, the PL generated electricity through the ICE and pyrolysis gas was used as an auxiliary fuel in the HRSG. We investigated the gas, liquid and solid pyrolytic products at a temperature of 550°C in the lab-scale SS pyrolysis apparatus. A schematic diagram of the energy flow of the SS pyrolysis process

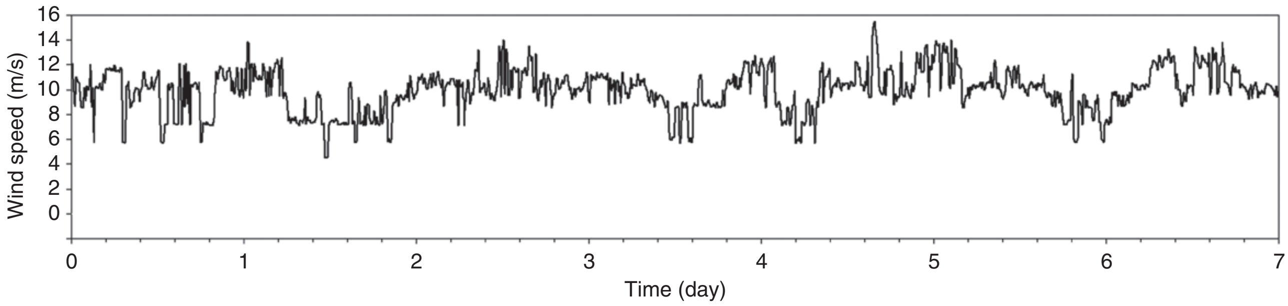

Fig. 3: Wind speed during the 7-day operation period.

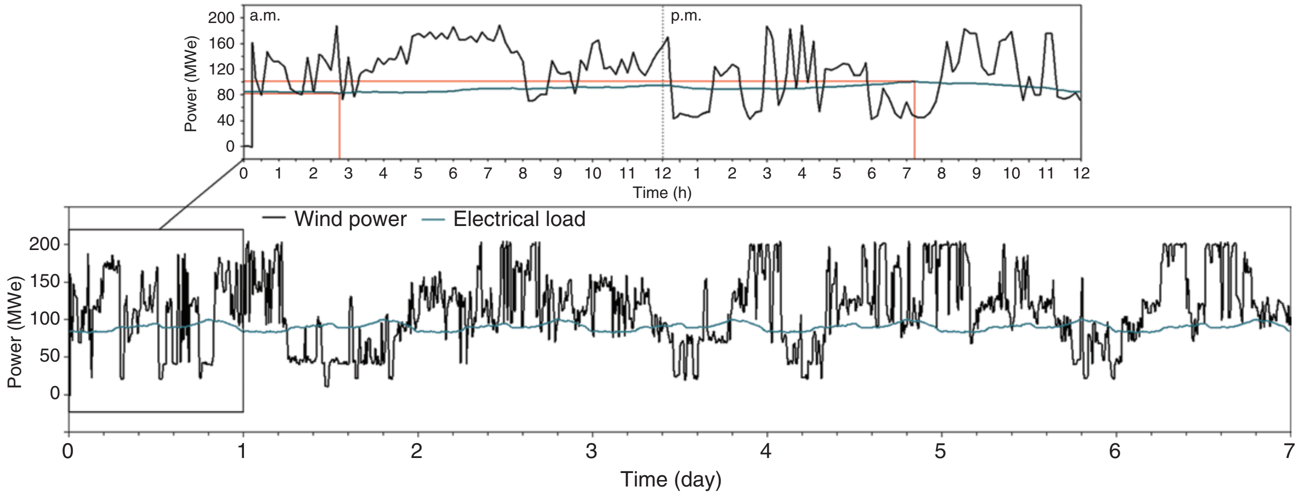

Fig. 4: Daily profiles of wind power generation and the electrical load during the 7-day operation.

Table 3: REMS design parameters

Parameters	Value
Wet SS daily disposal mass, t	1700
Moisture content, wt%	80
Dried SS daily production, t	362.71
Moisture content, wt%	6.26
Wind power plant rated capacity, MW$_e$	200
Initial wind-energy curtailment, %	30
CR of WPP system without ESS, %	88.66
Energy-utilization rate of the WPP system without ESS, %	70
Design performance of WPP system without ESS	62.06
CR of WPP system with ESS, %	100
Energy-utilization rate of WPP system with ESS, %	82.19
Design performance of WPP system with ESS	82.19
Wind-energy curtailment rate of WPP system with ESS, %	19.44
Rated capacity of ICE, MW$_e$	50
Power-generation efficiency of ICE, %	30
Efficiency of the heat-recovery steam generator, %	93
Rated capacity of EB, MW$_t$	40
Efficiency of EB, %	99
Effective capacity of batteries, %	90
Effective capacity of TES system, %	90
Initial state of charge of batteries	0.5
Initial state of charge of TES system	0.5
Calorific value of purchased fuel, MJ/kg	37

Table 4: Design parameters of the parametric study

Configured capacity of WPP, MW$_e$	Initial wind-curtailment rate, %	Maximum wind curtailment, %
125	10/20/28.07	28.07
150	10/20/30/40/40.07	40.07
175	10/20/30/40/48.61	48.61
200	10/20/30/40/50	50

was obtained and is shown in Fig. 5. The total energy recovered from solid, liquid and gas products was 32 420.85 kJ, representing 88.59% of the total input energy. The liquid product carried 2.22 and 3.85 times more energy than the solid and gas products, respectively. When deducting the sensible heat loss of each product, the energy balance error of 7.39% was caused by mass loss and measurement error. The error agreed the literature [38] for a small test bed.

In addition, the total PG and PL amounts accounted for 48.61 wt% of all the pyrolysis products. The calorific value of PG was 16.19 MJ/kg and PG had better fuel properties than the raw material. The calorific value of PL was 33.53 MJ/kg, which was much higher than the calorific value of the biomass pyrolysis oil product calorific value (19.92 MJ/kg) [39]. The results showed that PL and PG were suitable as alternative fuels. In addition, the relationship between the consumed and recovered energy during SS pyrolysis was applied to the REMS numerical modelling and provided design references for industrial-scale pyrolysis processes. Table 6 lists the detailed experimental results.

4.2 Performance of the REMS system

Fig. 6 shows the relationships between wind-power output and the REMS power demand with a rated WPP capacity of 200 MW$_e$ and an initial curtailment rate of 30%. Total power demand consisted of the electrical load and the electricity for SS pyrolysis and drying. Compared with Fig. 4, the power demand was increased by adding energy consumption during the pyrolysis process, and the input power to the EB directly addressed excess wind power, so more wind power generation was used, decreasing the wind-energy curtailment rate. Thus, the simulation of the system optimized the REMS-energy scheduling.

Fig. 7a shows that wind energy contributed the most electricity on demand and the power shortage caused by the variable nature of wind could be supplemented by ICE generation and discharged battery energy. However, the ICE-generated electrical energy could only satisfy the electricity needs on a relatively short time scale (e.g., during the period from 2.4 to 3.4 days) and the long-time-scale power gaps (e.g. the period from 1.2 to 2.0 days) should be filled by the joint power supply of the ICE and batteries. To guarantee on-demand electricity supply, the minimum battery storage capacity was estimated to be 0.95 GWh for 7-day operation. Fig. 7b shows the dispatching of the four heat sources for SS drying, including the recovered ICE heat, the stored heat, the heat supplied from PG combustion and the electrothermal conversion heat from the EB. The HRSG and TES facilities collectively provided >75% of the drying-heat demand. However, several heat gaps (<25% heat demand) still needed to be filled through EB electrothermal conversion. The maximum TES heat storage was 628.33 GJ, which ensured completely recovered excess-heat storage.

Fig. 8 gives the simulations of the battery operational behaviour. Total power demand was used as the threshold to make decisions on wind-power dispatch. The excess power was charged into the batteries when the wind power could satisfy the requirements and the power gaps were filled by the discharged battery power if the wind power could not meet the total power demand. The battery-charge state changed with the charge and discharge operations as shown in Fig. 8. During the specific short periods on the fifth and sixth days (Day 5.49–5.54, 5.55–5.57, 5.64–5.65, 6.62–6.65, 6.66–6.69, 6.73–6.77, 6.79–6.81, 6.83–6.84, 6.85–6.88, 6.92–6.95 and 6.99–7.00), the SOC was maintained at the maximum value, meaning that the batteries were fully charged. At that time, the excess wind power was curtailed. In Fig. 8b, the grey shadows within these time periods are marked as the curtailed wind energy caused by the storage-scale limitation.

Table 5: Unit costs of devices and fuels

Parameters	Value
Wet SS unit mass disposal subsidy, $/t	30
Effective soil-remediation unit cost, $/m^2	15
Biochar effective soil-remediation coefficient, m^2/t	670
CO_2 emissions unit cost, $/t	46
CO_2 emission factor per energy generation, t/MWh	0.97
Pyrolytic fuel CO_2 emission factor per energy consumption, t/GJ	0.067
Purchased fuel CO_2 emission factor per energy consumption, t/GJ	0.073
WPP capital cost, $/MW$_e$	1 400 000
Electrochemical storage (battery) capital cost, $/MWh	195 000
TES capital cost, $/GJ	4170
Pyrolytic fuel price, $/GJ	9.88
Extra-purchased fuel price, $/GJ	21
Electricity price, $/MWh	80

The total rate of REMS-energy utilization was quite high at 99.23% (Table 7) and provided the energy demands for both electricity supply and SS pyrolysis. The energy loss was mainly due to limitations in battery capacity and the energy-conversion efficiency of each unit. Due to operational constraints, there was some energy left in the batteries and fuel storage tanks for later use. Compared with the WPP system without any flexible

Table 6: Sewage sludge pyrolysis results at 550°C

Parameter	Value
Total energy input, kJ	36 595.82
Energy of feedstock, kJ	26 153.82
Feedstock mass, g	1,998.00
Net energy consumption during pyrolysis, kJ	10 442.00
Energy of gas product, kJ	4916.86
Gas-product calorific value, kJ/m^3	21 386.94
Gas-product volume, L	229.90
Gas-product yield, wt%	20.35
Energy of liquid product, kJ	18 931.04
Liquid-product calorific value, kJ/kg	33 530.00
Liquid-product mass, g	564.60
Liquid-product yield, wt%	28.26
Energy of solid product, kJ	8572.95
Solid-product calorific value, kJ/kg	8350.00
Solid-product mass, g	1026.70
Solid-product yield, wt%	51.39
Carbon content, wt%	22.17
Total recyclable energy[a], kJ	32 420.85
Total energy-recovery efficiency[b], %	88.59
Useable energy efficiency[c], %	73.56
Sensible energy loss[d] of gas production, kJ	252.44
Sensible energy loss of liquid production, kJ	718.17
Sensible energy loss of solid production, kJ	550.62
Percentage of total sensible energy loss[e], %	4.02
Balance error[f], %	7.39

[a] Sum of the energy of gas, liquid and solid products.
[b] The ratio of total recyclable energy and the total energy input.
[c] The ratio between the sum of the energy of gas and liquid products and the total energy input.
[d] Sensible energy loss (kJ) = $c_p m \Delta T$, where c_p, m and ΔT represent the specific heat, mass and temperature change of the subject.
[e] The ratio between the sum of the sensible energy loss of gas, liquid and solid products and the total energy input.
[f] Balance error (%) = 100 % – total energy-recovery efficiency percent of total sensible energy loss.

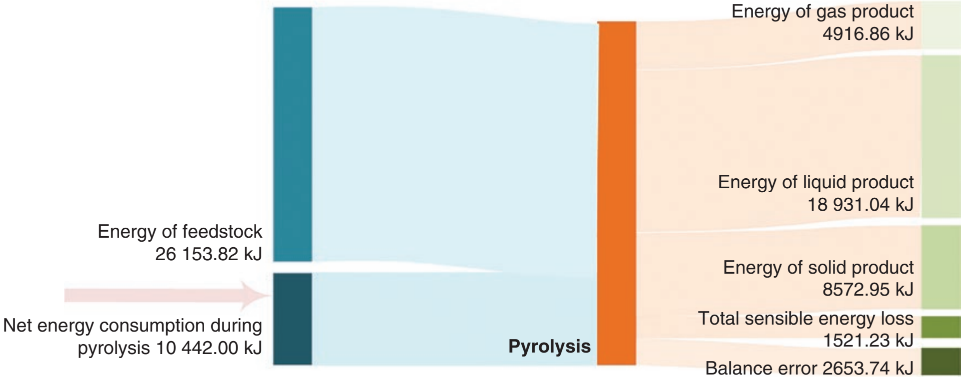

Fig. 5: Schematic diagram of the energy flow of the sewage sludge pyrolysis process at 550°C.

dispatching devices, the REMS wind-energy curtailment rate was reduced from 30% to 0.78%, and the performance of the integrated system increased from 62.06 to 99.23. Even if the WPP system was equipped with an ESS, the system retained a wind curtailment of 19.44% and the design performance score was 82.19. This indicated that integrating WPP with StE effectively improved the safety and flexibility of wind-energy use and demonstrated good applicability for energy dispatch.

4.3 Influence of the wind-curtailment rate and WPP scale

We conducted a parametric analysis to investigate the influences of the initial wind-curtailment rate and the configuration of the WPP capacity on the REMS system performance (see Table 4). Fig. 9 shows the CR of the variations in the electricity supply and the energy-utilization rate caused by the initial wind curtailment with different configured WPP capacities (125, 150, 175 and 200 MW_e). There was an upward trend of CR with increasing initial wind-curtailment rate φ_{cur} (Fig. 9a). When the REMS was at the same wind-curtailment rate, the larger the WPP configured capacity, the higher the CR. We also found that the CR of the system with configured capacities of 200 and 175 MW_e started to level off at 100% when the initial wind-curtailment rate φ_{cur} rose from 10% to 27.87% and 32.00%, respectively. The integrated system could not achieve a complete electricity supply when the configured WPP capacity was designed at 150 and 125 MW_e. That is because the WPP capacities of 150 and 125 MW_e are too small for this integrated system when the initial wind-curtailment rates are set over 40.07% and 28.07%. Under these conditions, the integrated system can achieve full power operation with the maximum electricity supply completion rates of 99.66% and 86.48% respectively. Then the total wind power and the initial curtailment rate will not increase with the wind speed, and there are only four data points for the case of 150 MW_e and three data points for the case of 125 MW_e. Usually, a larger wind-curtailment rate means a higher wind speed. Both the higher wind speed and the larger WPP scale were helpful in meeting the power demand. On the contrary, the electrical generation of a small-scale WPP (such as 125 and 150 MW_e) with less wind was insufficient. Fig. 9b shows that as φ_{cur} increased to a certain value and the configured WPP scale was large enough, the REMS-energy utilization rate decreased from the stable state of 100% (e.g. when $I_{Cp,wind}$ was set as 200 MW_e and φ_{cur} grew to 27.87%). Excess generation reduced the level of energy use. As discussed, critical system performance points could be determined, at which the systematic CR of the electricity supply and energy-utilization rate reached 100%, such as when $\varphi_{cur} = 27.87\%$ and $I_{Cp,wind} = 200$ MW_e and when $\varphi_{cur} = 32.00\%$ and $I_{Cp,wind} = 175$ MW_e.

The design performance index Ω_{design} was used to further demonstrate the influence of WPP configurations on system

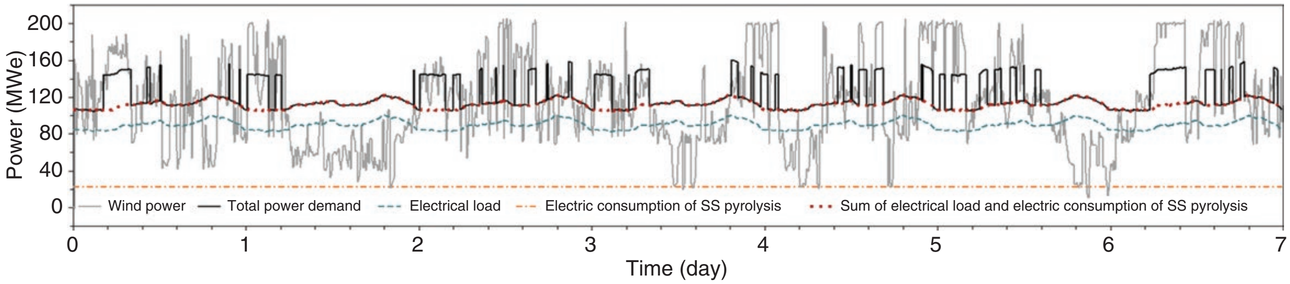

Fig. 6: Daily profiles of wind power and electricity demands after equipping with the sludge-to-energy process.

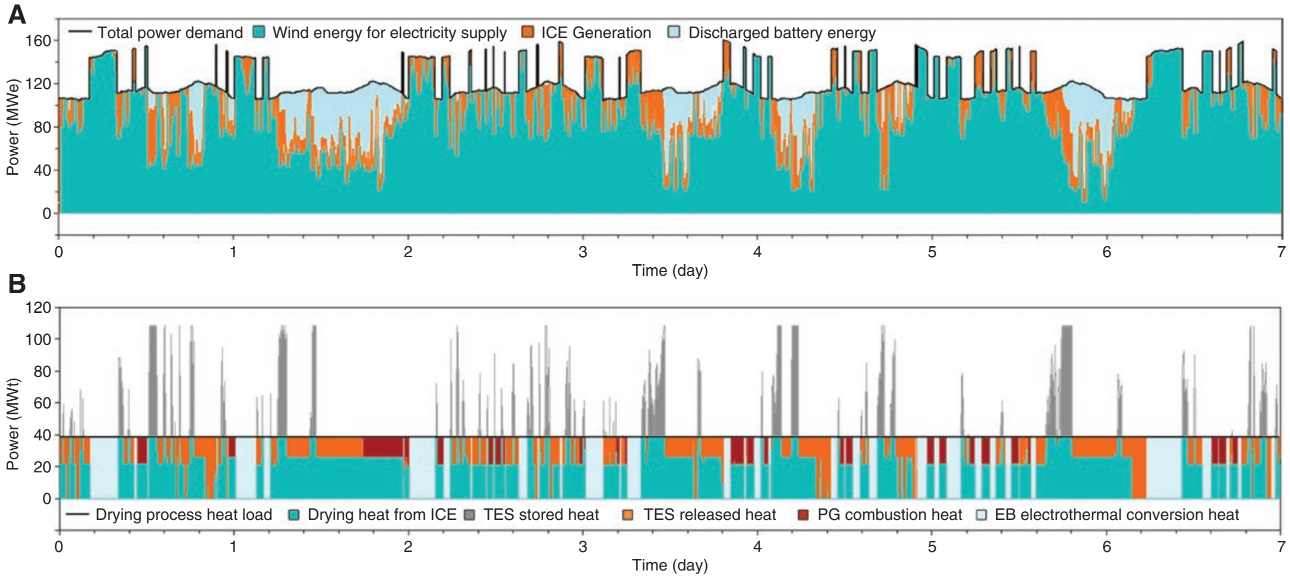

Fig. 7: The simulated result of the energy scheduling for (a) electricity demand and (b) heat demand in the REMS.

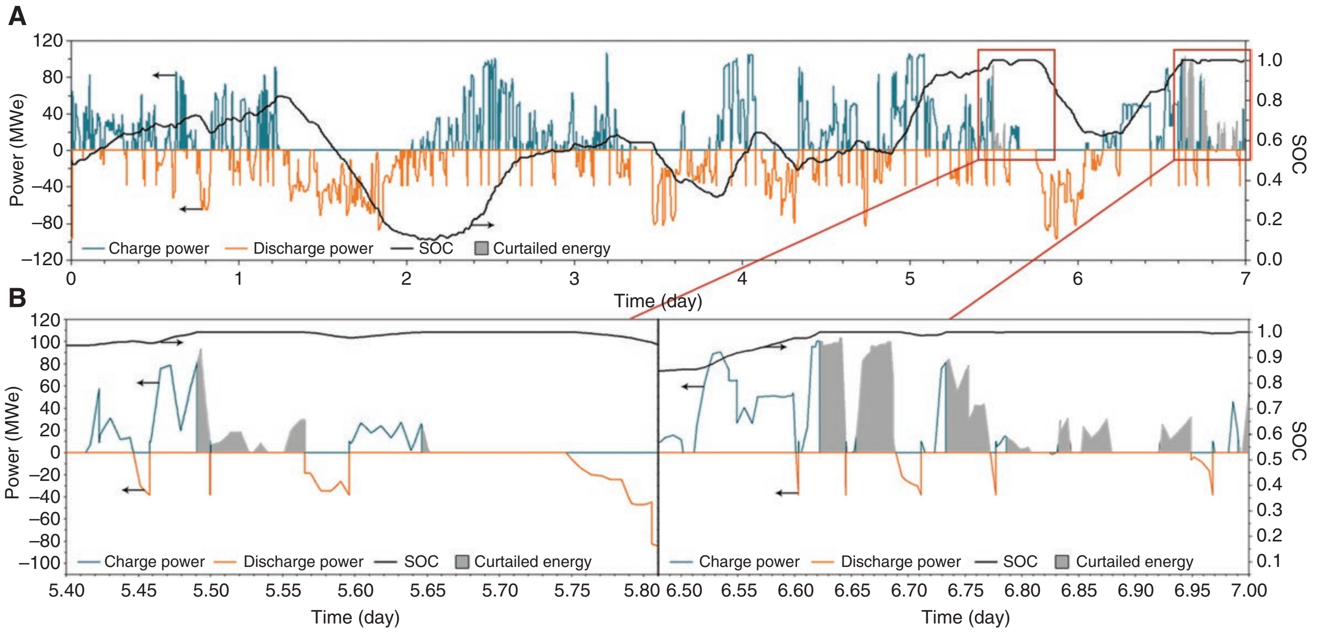

Fig. 8: Battery charge and discharge behaviours in (a) full view and (b) local view.

performance under different wind sources. For this purpose, the contour map (Fig. 10) is used to show the relationship among the parameters Ω_{design}, φ_{cur} and $I_{Cp,wind}$. It also provides a design reference for optimizing the configuration. The valid range of design parameters (φ_{cur} and $I_{Cp,wind}$) is marked as the area ABCD, located in the coordinate frame that excludes the solid-line-covered triangle. When $I_{Cp,wind}$ was <153 MW_e, the design performance index increased with φ_{cur}. When $I_{Cp,wind}$ was >153 MW_e, the design performance index also increased with φ_{cur} and when it reached the maximum value, it showed the opposite trend. Accordingly, REMS with a design performance index (Ω_{design}) of 100 could be used as the optimal system configuration design with different WPP capacities and wind sources. Table 7 records the results of the system performance simulation with the optimal configurations. The initial rate of wind curtailment of the optimum configuration was in the range of 27.87–34.12% (the corresponding WPP capacity was in the range of 200–155 MW_e), all of which were wind-rich and had a low match between electricity supply and demand. The result showed that in these scenarios, the total wind generation remained at ~19 GWh and the electricity that must be supplied by the ICE and batteries was ~4 GWh. This suggested that there would be good performance in the 7-day REMS operation with a daily wet SS disposal requirement of 1700 tons when the daily total wind-energy generation was ~2.71 GWh and on-demand electricity accounted for ~70% of the wind generation.

Table 7: Results of the system performance simulation during 7-day operation period

Key performance parameters	Value
Wet SS disposal mass, t	11 900
Dried SS disposal mass, t	2538.97
Total wind energy, GWh	19.13
End-user electricity demand, GWh	15.10
Electricity for driving pyrolysis, GWh	3.72
SS drying heat, GJ	23 121.50
ICE electricity generation, GWh	1.93
PL heat generation, GJ	15 067.30
PG heat generation, GJ	2131.73
Net storage PL mass, t	48.24
Net storage PG mass, t	259.62
Net storage electricity, GWh	0.95
Purchased fuel mass, t	64.53
Purchased electricity, GWh	0
Minimum battery capacity, GWh	0.95
Minimum TES capacity, GJ	628.33
Pyrolytic char mass, t	1304.67
REMS electricity supply CR, %	100
REMS-energy utilization rate, %	99.23
REMS wind-energy curtailment, %	1.24
REMS design performance index	99.23

4.4 Environmental and economic analysis

Using the simulations in Section 4.2 and the case settings in Section 3.2.4, the REMS disposal approach using renewable energy (wind power and pyrolysis products) to replace conventional coal-fired power plants could achieve monetized environmental benefits of $14 081 665. This design also reduced CO_2 emissions by ~13 320 tons and provided effective soil remediation for 874 129 m^2. This result illustrated that the integrated system had important implications for the disposal and management of SS, the reduction of GHG emissions, the replacement of fossil fuels and the development potential in the social economy.

The parameter F_{REMS} used to represent the economic effects of the optimized configurations was calculated according to the REMS parametric study results in Section 4.3. Fig. 11

provides the fitted F_{REMS} curve, which first rose and then declined with increasing configured WPP capacity. The corresponding factors that influenced F_{REMS} are also shown in the figure as the column chart. The system needed little or no grid energy and the minimum F_{REMS} value appeared when the optimum WPP configuration was the smallest. This meant that REMS could achieve the best economy when $I_{Cp,wind}$ = 155 MW_e and φ_{cur} = 34.12%. In addition, the column chart reveals that the electricity-storage scale had the greatest impact on F_{REMS} among the various factors. It also shows that the REMS cost control depended, in turn, upon a further reduction in the electricity-storage cost.

5 Conclusions

SS resource recovery involves the sustainable development of energy, the environment and the economy. In this study, we analysed the applicability of the SS pyrolysis process in a renewable-energy microgrid. We conducted experiments to investigate the three-phase pyrolytic product yields and the SS pyrolysis mass and energy balances at 550°C. We developed an integrated wind–StE power system REMS based on SS characteristics and pyrolysis performance. The system was evaluated on a 7-day continuous operation. We studied the influence of WPP capacity on the REMS performance under different wind sources. Environmental and economic benefits were also discussed. We offer the following main conclusions.

After pyrolysis, the calorific values of PG and PL were tested as 16.19 and 33.53 MJ/kg, which are better than those of the raw material. It means that the gaseous and liquid SS pyrolytic products are capable of being used as chemical-energy storage in renewable-energy microgrids. The pyrolysis char could be used in soil remediation to increase the environmental and economic benefits of REMS.

The proposed REMS synergized wind power and the SS pyrolysis process while providing on-demand power services to customers in specific areas. Wind power could drive the continuous operation of the pyrolysis process. SS pyrolysis fuel products were used for power and heat supply to compensate for fluctuations in the power and drying-heat consumption. When the WPP capacity was 200 MW_e and the initial wind-energy curtailment rate was 30%, the integrated system performance was increased from 62.06 to 99.23 by REMS. The integrated system increased wind-energy utilization, reused SS and significantly improved environmental benefits.

The integrated REMS could achieve 100% energy utilization and 100% electricity supply CR within the configured WPP capacity range of 155–200 MW_e. The larger the WPP capacity, the lower the initial wind curtailment. The REMS was also economically feasible. The F_{REMS} variation revealed that the difference in the economic cost was mainly affected by the scale of the electricity-storage device. The optimal REMS design was obtained when $I_{Cp,wind}$ = 155 MW_e and φ_{cur} = 34.12%. By this design scheme, the integrated system could meet end-user electricity demands of 15.10 GWh and the daily disposal of 1700 wet tonnes of SS, as well as improve wind-energy curtailment.

In summary, REMS has good prospects for integrating SS pyrolysis technology and renewable energy, and helps to realize carbon-neutral energy-generation goals. The long-term evaluation of the system operation should be performed with actual engineering data, especially with the life cycle of the storage system and involved facility maintenance.

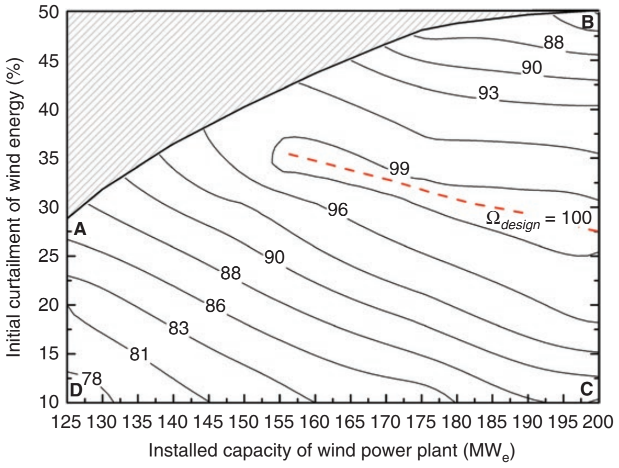

Fig. 10. REMS design performance index.

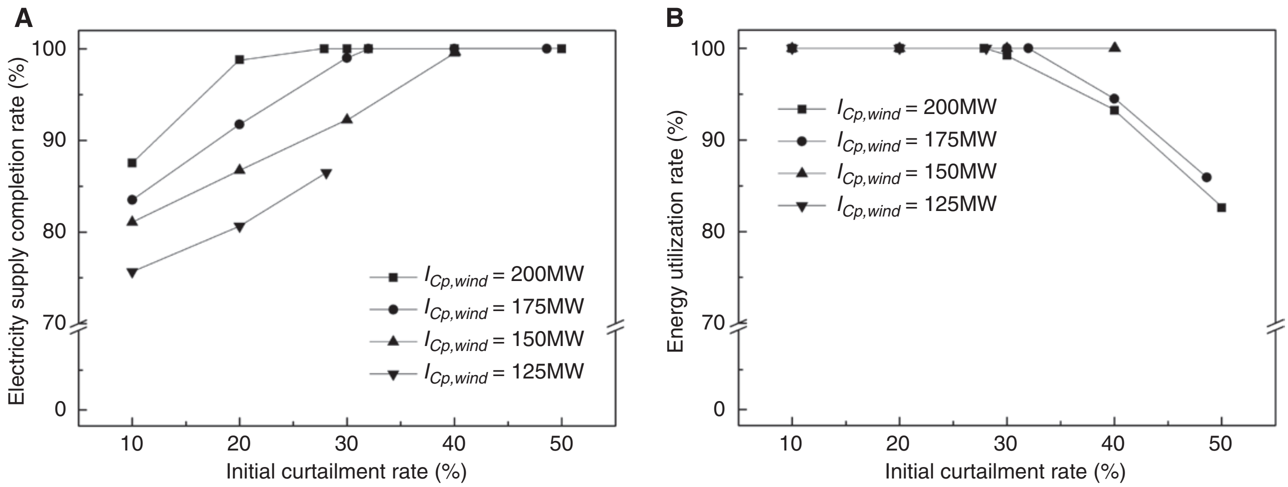

Fig. 9: Evolution of REMS system performance under different initial wind-curtailment rates and configured WPP capacities, including (a) the CR of the electricity supply and (b) the energy-utilization rate.

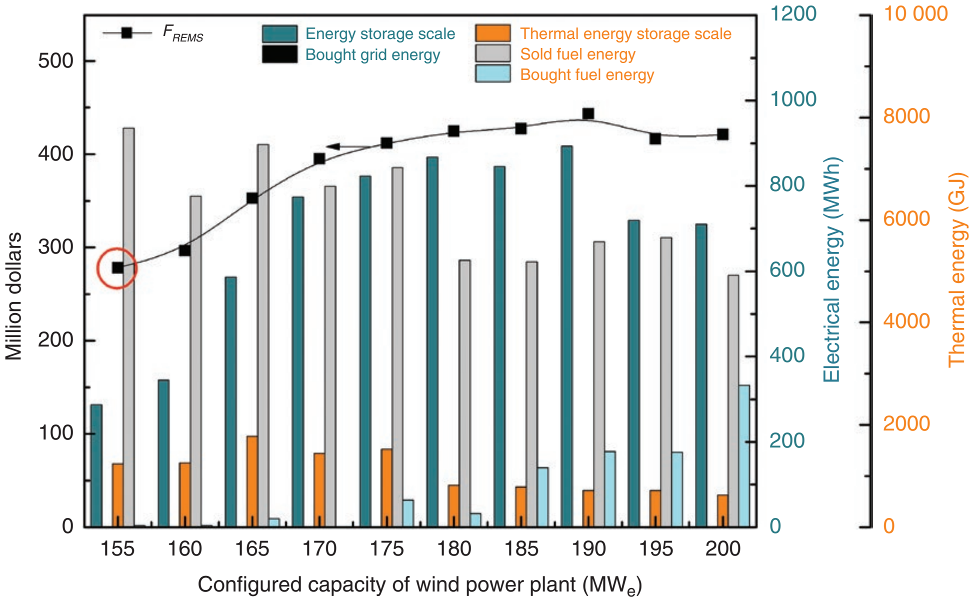

Fig. 11. Economic factors of the optimal REMS configurations.

Nomenclature

$c_{subsidy}$: disposal subsidy of unit mass of SS, \$/t
c_{soil}: unit cost of effective soil remediation, \$/m^2
$c_{emission}$: unit cost of CO_2 emissions, \$/t
c_{wind}: capital cost of wind power plant, \$/MW$_e$
c_B: capital cost of battery, \$/MWh
c_{TES}: capital cost of TES system, \$/GJ
$c_{fuel,pyr}$: price of the redundant pyrolytic fuels, \$/GJ
$c_{fuel,pur}$: price of the extra-purchased fuel, \$/GJ
c_e: price of electricity, \$/MWh
$C_{subsidy}$: financial subsidy of SS disposal, \$
C_{soil}: benefit of soil remediation, \$
$C_{emission}$: benefit of mitigation of CO_2 emission, \$
C_{cons}: construction cost of REMS, \$
C_{sell}: total operational income of REMS, \$
C_{buy}: expense of purchased fuel and electricity, \$
$E_{TES,net}$: net storage energy of TES, GJ
$E_{B,net}$: net storage energy of battery, MWh
E_{StE}: total energy of utilized PL and PG, GJ
$E_{pur,total}$: total purchased energy, GJ
F_{REMS}: revenue and expenditure of the REMS, \$
H: calorific value, MJ/kg
$I_{Cp,TES}$: configured capacity of TES system, GJ
$I_{Cp,B}$: configured capacity of battery, MWh
$I_{Cp,wind}$: capacity of wind power plant, MW$_e$
M: mass, t
P: power, MW$_e$ or MW$_t$
SOC: state of charge
t: operating time, s
t_c: a certain time, s
T: operation period, s
Y: yield of pyrolysis product, wt%
ΔE: change of energy, MWh or GJ
ΔP: power difference, MW$_e$ or MW$_t$

Greek symbols

δ_E: completion rate of electricity supply, %
δ_U: energy-utilization rate, %
ζ: CO_2 emission factor, t/MWh or t/GJ
η: efficiency, %
φ: curtailment rate of wind energy, %
Ω_{design}: index of design performance

Subscripts

act: actual
B: battery
charge: charge
cur: curtailment of wind energy
demand: demand power or demand energy
discharge: discharge
drying: sewage sludge drying
e: electricity
fuel: fuel
grid: utility grid
i: fuel species
input: input
j: storage period
load: electricity load
max: maximum
min: minimum
net: net storage energy
pur: purchase
pyr: pyrolysis
th: thermal
total: total
wind: wind power

Funding

This work was supported by the National Key Research and Development Program of China (2019YFE0100100). There is no room to add a funding section in the manuscript.

Conflict of interest statement

None declared.

References

[1] Gao NB, Kamran K, Quan C, *et al*. Thermochemical conversion of sewage sludge: a critical review. *Prog Energy Combust Sci*, 2020, 79:1008431–1008438. doi:10.1016/j.pecs.2020.100843.

[2] Zhu XF, Yuan WY, Lang MQ, *et al*. Novel methods of sewage sludge utilization for photocatalytic degradation of tetracycline-containing wastewater. *Fuel*, 2019, 252:148–156. doi:10.1016/j.fuel.2019.04.093.

[3] Wu BR, Dai XH, Chai XL. Critical review on dewatering of sewage sludge: influential mechanism, conditioning technologies and implications to sludge re-utilizations. *Water Res*, 2020, 180:1159121–1159118. doi:10.1016/j.watres.2020.115912.

[4] Madon I, Drev D, Likar J. Long-term risk assessments comparing environmental performance of different types of sanitary landfills. *Waste Manage*, 2019, 96:96–107. doi:10.1016/j.wasman.2019.07.001.

[5] Awasthi MK, Pandey AK, Khan J, *et al*. Evaluation of thermophilic fungal consortium for organic municipal solid waste composting. *Bioresour Technol*, 2014, 168:214–221. doi:10.1016/j.biortech.2014.01.048.

[6] Jayaraman K, Goekalp I. Pyrolysis, combustion and gasification characteristics of miscanthus and sewage sludge. *Energy Convers Manage*, 2015, 89:83–91. doi:10.1016/j.enconman.2014.09.058.

[7] Lee RP, Meyer B, Huang Q, *et al*. Sustainable waste management for zero waste cities in China: potential, challenges and opportunities. *Clean Energy*, 2020, 4:169–201. doi:10.1093/ce/zkaa013.

[8] Do TX, Mujahid R, Lim HS, *et al*. Techno-economic analysis of bio heavy-oil production from sewage sludge using supercritical and subcritical water. *Renew Energy*, 2020, 151:30–42. doi:10.1016/j.renene.2019.10.138.

[9] Bando S, Asano H, Sasajima K, Odajima N, Sei M, Ogata T. Optimal configuration of energy supply system in a microgrid with steam supply from a municipal waste incinerator. In: *8th International Conference on Power Electronics—ECCE Asia*, Jeju, Korea, 30 May 2011–3 June 2011, 557–564. doi:10.1109/ICPE.2011.5944605.

[10] Li LY, You SM, Wang XN. Optimal design of standalone hybrid renewable energy systems with biochar production in remote rural areas: a case study. In: Yan J, Yang HX, Li H, Chen X (eds). *Innovative Solutions for Energy Transitions*. Amsterdam: Elsevier, 2019, 688–693. doi:10.1016/j.egypro.2019.01.185.

[11] Perna A, Minutillo M, Lavadera AL, *et al*. Combining plasma gasification and solid oxide cell technologies in advanced power plants for waste to energy and electric energy storage applications. *Waste Manage*, 2018, 73:424–438. doi:10.1016/j.wasman.2017.09.022.

[12] Ruya PM, Purwadi R, Lim SS. Supercritical water gasification of sewage sludge for power generation: thermodynamic study on auto-thermal operation using Aspen Plus. *Energy Convers Manage*, 2020, 206:112458. doi:10.1016/j.enconman.2019.112458.

[13] Sobek S, Werle S. Solar pyrolysis of waste biomass. Part 1: Reactor design. *Renew Energy*, 2019, 143:1939–1948. doi:10.1016/j.renene.2019.06.011.

[14] Liu C, Zhang Z, Liu W, *et al*. Flow fuel cell powered by combustible agricultural waste. *Clean Energy*, 2018, 2:20–28. doi:10.1093/ce/zky001.

[15] Bora AP, Gupta DP, Durbha KS. Sewage sludge to bio-fuel: a review on the sustainable approach of transforming sewage waste to alternative fuel. *Fuel*. 2020, 259:25. doi:10.1016/j.fuel.2019.116262.

[16] Ameri B, Hanini S, Benhamou A, *et al*. Comparative approach to the performance of direct and indirect solar drying of sludge from sewage plants, experimental and theoretical evaluation. *Sol Energy*, 2018, 159:722–732. doi:10.1016/j.solener.2017.11.032.

[17] Wang P, Mohammed D, Zhou P, *et al*. Roof solar drying processes for sewage sludge within sandwich-like chamber bed. *Renew Energy*, 2019, 136:1071–1081. doi:10.1016/j.renene.2018.09.081.

[18] Li X, Shen Y, Wei L, *et al*. Hydrogen production of solar-driven steam gasification of sewage sludge in an indirectly irradiated fluidized-bed reactor. *Appl Energy*, 2020, 261:114229. doi:10.1016/j.apenergy.2019.114229.

[19] Kokalj F, Arbiter B, Samec N. Sewage sludge gasification as an alternative energy storage model. *Energy Convers Manage*, 2017, 149:738–747. doi:10.1016/j.enconman.2017.02.076.

[20] Calise F, Di Fraia S, Macaluso A, *et al*. A geothermal energy system for wastewater sludge drying and electricity production in a small island. *Energy*, 2018, 163:130–143. doi:10.1016/j.energy.2018.08.062.

[21] BP. *Statistical Review of World Energy 2020*. https://www.bp.com/content/dam/bp/business-sites/en/global/corporate/pdfs/energy-economics/statistical-review/bp-stats-review-2020-full-report.pdf (27 October 2020, date last accessed).

[22] Baran B, Mamis MS, Alagoz BB. Utilization of energy from waste plants for microgrids. In: *2016 4th International Istanbul Smart Grid Congress and Fair*, Istanbul, Turkey, 20–21 April 2016, 131–135. doi:10.1109/SGCF.2016.7492431.

[23] Perkins G. Integration of bio crude production from fast pyrolysis of biomass with solar PV for dispatchable electricity production. *Clean Energy*, 2018, 2:85–101. doi:10.1093/ce/zky013.

[24] Kern S, Halwachs M, Kampichler G, *et al*. Rotary kiln pyrolysis of straw and fermentation residues in a 3 MW pilot plant: influence of pyrolysis temperature on pyrolysis product performance. *J Anal Appl Pyrolysis*, 2012, 97:1–10. doi:10.1016/j.jaap.2012.05.006.

[25] Pröll T, Afif RA, Schaffer S, *et al*. Reduced local emissions and long-term carbon storage through pyrolysis of agricultural waste and application of pyrolysis char for soil improvement. *Energy Procedia*, 2017, 114:6057–6066. doi:10.1016/j.egypro.2017.03.1742.

[26] Roy P, Dias G. Prospects for pyrolysis technologies in the bioenergy sector: a review. *Renew Sustain Energy Rev*, 2017, 77:59–69. doi:10.1016/j.rser.2017.03.136.

[27] Saadi W, Rodríguez-Sánchez S, Ruiz B, *et al*. Pyrolysis technologies for pomegranate (Punica granatum L.) peel wastes: prospects in the bioenergy sector. *Renew Energy*, 2019, 136:373–382. doi:10.1016/j.renene.2019.01.017.

[28] Eberhart P, Chung TS, Haumer A, Kral C. Open source library for the simulation of wind power plants. In: *The 11th International Modelica Conference,* Versailles, France, 21–23 September 2015, 929–936. doi:10.3384/ecp15118929.

[29] Das S, Lee SH, Kumar P, *et al*. Solid waste management: scope and the challenge of sustainability. *J Clean Prod*, 2019, 228:658–678. doi:10.1016/j.jclepro.2019.04.323.

[30] Vermont Department of Environmental Conservation. *Waste Treatment Sludge and Septage Management in Vermont*. https://dec.vermont.gov/sites/dec/files/wmp/residual/RMSWhitePaper.pdf (30 October 2020, date last accessed).

[31] Gillingham K, Stock JH. The cost of reducing greenhouse gas emissions. *J Econ Perspect*, 2018, 32:53–72. doi:10.1257/jep.32.4.53.

[32] Kim Y, Parker W. A technical and economic evaluation of the pyrolysis of sewage sludge for the production of bio-oil. *Bioresour Technol*, 2008, 99:1409–1416. doi:10.1016/j.biortech.2007.01.056.

[33] Qian L, Wang S, Savage PE. Fast and isothermal hydrothermal liquefaction of sludge at different severities: reaction products, pathways, and kinetics. *Appl Energy*, 2020, 260:11431210. doi:10.1016/j.apenergy.2019.114312.

[34] Meng A, Zhang Y, Zhuo J, *et al*. Investigation on pyrolysis and carbonization of Eupatorium adenophorum Spreng and tobacco stem. *J Energy Inst*, 2015, 88:480–489. doi:10.1016/j.joei.2014.10.003.

[35] Gao B, Wei L, Long L. Experimental study on pyrolysis process of sewage sludge and its gas producing characteristics. *Zaisheng Ziyuan Yanjiu*, 2007, 2:40–43 (in Chinese).

[36] García AN, Marcilla A, Font R. Thermogravimetric kinetic study of the pyrolysis of municipal solid waste. *Thermochim Acta*, 1995, 254:277–304. doi:10.1016/0040-6031(94)02002-6.

[37] Suntivarakorn R, Treedet W, Singbua P, *et al*. Fast pyrolysis from Napier grass for pyrolysis oil production by using circulating fluidized bed reactor: improvement of pyrolysis system and production cost. *Energy Rep*, 2018, 4:565–575. doi:10.1016/j.egyr.2018.08.004.

[38] Karaca C, Sozen S, Orhon D, *et al*. High temperature pyrolysis of sewage sludge as a sustainable process for energy recovery. *Waste Manage*, 2018, 78:217–226. doi:10.1016/j.wasman.2018.05.034.

[39] Ning S-K, Hung M-C, Chang Y-H, *et al*. Benefit assessment of cost, energy, and environment for biomass pyrolysis oil. *J Clean Prod*, 2013, 59:1419–1149. doi:10.1016/j.jclepro.2013.06.042.